Wang, Honglei; Jiao, Yunfei; Wu, Bing; Wang, Dong; Hu, Yueqi; Liang, Fei; Shen, Chen; Knauer, Andrea; Ren, Dan; Wang, Hongguang; Aken, Peter Antonie van; Zhang, Hongbin; Sofer, Zdenek; Grätzel, Michael; Schaaf, Peter

Exfoliated 2D layered and nonlayered metal phosphorous trichalcogenides nanosheets as promising electrocatalysts for CO2 reduction

Original published in:	Angewandte Chemie. International edition / Gesellschaft Deutscher Chemiker - Weinheim : Wiley-VCH. - 62 (2023), 17, art. e202217253, 8 pp.
Original published:	2023-02-06
ISSN:	1521-3773 ; 1433-7851
DOI:	10.1002/anie.202217253
[*Visited:*	2023-07-18]

How to cite: *Angew. Chem. Int. Ed.* **2023,** *62,* e202217253
International Edition: doi.org/10.1002/anie.202217253
German Edition: doi.org/10.1002/ange.202217253

CO_2 Reduction

Exfoliated 2D Layered and Nonlayered Metal Phosphorous Trichalcogenides Nanosheets as Promising Electrocatalysts for CO_2 Reduction

Honglei Wang[+], Yunfei Jiao[+], Bing Wu, Dong Wang, Yueqi Hu, Fei Liang, Chen Shen,* Andrea Knauer, Dan Ren,* Hongguang Wang,* Peter A. van Aken, Hongbin Zhang, Zdenek Sofer, Michael Grätzel, and Peter Schaaf*

Abstract: Two-dimensional (2D) materials catalysts provide an atomic-scale view on a fascinating arena for understanding the mechanism of electrocatalytic carbon dioxide reduction (CO_2 ECR). Here, we successfully exfoliated both layered and nonlayered ultra-thin metal phosphorous trichalcogenides ($MPCh_3$) nanosheets via wet grinding exfoliation (WGE), and systematically investigated the mechanism of $MPCh_3$ as catalysts for CO_2 ECR. Unlike the layered $CoPS_3$ and $NiPS_3$ nanosheets, the active Sn atoms tend to be exposed on the surfaces of nonlayered $SnPS_3$ nanosheets. Correspondingly, the nonlayered $SnPS_3$ nanosheets exhibit clearly improved catalytic activity, showing formic acid selectivity up to 31.6% with $-7.51\,mA\,cm^{-2}$ at $-0.65\,V$ vs. RHE. The enhanced catalytic performance can be attributed to the formation of HCOO* via the first proton-electron pair addition on the $SnPS_3$ surface. These results provide a new avenue to understand the novel CO_2 ECR mechanism of Sn-based and $MPCh_3$-based catalysts.

Introduction

Electrocatalytic carbon dioxide reduction (CO_2 ECR), which harvests CO_2 as value-added chemicals and fuels using renewable electricity, provides a promising avenue to alleviating carbon emissions.[1] Formic acid (HCOOH), as a liquid hydrogen carrier with high energy density ($1.77\,kWh\,L^{-1}$) and hydrogen load (4.35% of its weight), plays an important role in the chemical industry as a feedstock.[2] Thus, out of many possible products in CO_2 ECR, there is a strong impetus to search for promising materials with good selectivity, high activity, and robust stability for formic acid productions (and other desired products). Sn-based materials have been demonstrated as promising catalysts for electrocatalytic CO_2-to-formic acid conversion, also given their earth-abundant, eco/env-friendly characteristics.[3] Up to now, a variant form of Sn-based catalysts have been studied for CO_2 ECR, e.g., single metals, alloys, metal oxides, and carbon hybrids materials.[4] Moreover, more types and morphologies of Sn-based catalysts need further study. Two-dimensional (2D) materials with atomic-scale thicknesses as candidate CO_2 ECR catalysts have shown excellent catalytic activities owing to their high electrical conductivity, amply exposed surface atoms, and high specific surface area.[5] Additionally, the well-controlled

[*] H. Wang,[+] Dr. D. Wang, Y. Hu, Prof. Dr. P. Schaaf
Chair Materials for Electrical Engineering and Electronics, Institute of Materials Science and Engineering and Institute of Micro and Nanotechnologies MacroNano, TU Ilmenau
Gustav-Kirchhoff-Str. 5, 98693 Ilmenau (Germany)
E-mail: dong.wang@tu-ilmenau.de

Dr. Y. Jiao,[+] Prof. Dr. D. Ren, Prof. Dr. M. Grätzel
Laboratory of Photonics and Interfaces, École Polytechnique Fédérale de Lausanne
1015 Lausanne (Switzerland)

B. Wu, Prof. Dr. Z. Sofer
Department of Inorganic Chemistry, University of Chemistry and Technology Prague
Technická 5, 166 28 Prague 6 (Czech Republic)

Prof. Dr. F. Liang, Dr. C. Shen, Prof. Dr. H. Zhang
Institut für Materialwissenschaft, Technische Universität Darmstadt
64289 Darmstadt (Germany)
E-mail: chenshen@tmm.tu-darmstadt.de

Dr. A. Knauer
Institute of Micro- and Nanotechnologies MacroNano®, TU Ilmenau
Gustav-Kirchhoff- Str.7, 98693 Ilmenau (Germany)

Prof. Dr. D. Ren
School of Chemical Engineering and Technology, Xi'an Jiaotong University
Xi'an 710049 (P. R. China)
E-mail: dan.ren@xjtu.edu.cn

Dr. H. Wang, Prof. Dr. P. A. van Aken
Max Planck Institute for Solid State Research
Heisenbergstr. 1, 70569 Stuttgart (Germany)
E-mail: hgwang@fkf.mpg.de

[+] These authors contributed equally to this work.

crystal structures of 2D materials benefit the understanding of the atomic-scale relationships between active sites and reactivity for CO_2 ECR.[6] However, 2D metal nanosheets are prone to oxidation, leading to a rapid loss of cyclability.[7] Moreover, exploring 2D transition-metal dichalcogenides (TMDs) as catalysts demands the use of an ionic liquid as the electrolyte; otherwise, the hydrogen evolution reaction (HER) will surpass the CO_2 reduction during the CO_2 ECR.[8] Therefore, it is worthwhile exploring new types of 2D nanosheets to produce carbon products such as formic acid through CO_2 ECR, with good selectivity against other competitive reactions.

Metal-phosphorus-chalcogen (MPCh) complexes offer a wide range of layered compounds with a vast spectrum of potential applications, with metal phosphorous trichalcogenides ($MPCh_3$) being the most widely studied.[9] Generally, the $MPCh_3$ materials are categorized into two classes based on the interlayer forces. On one hand, both P_2 pairs and metal atoms are in octahedral coordination and van der Waals forces can stack the layers to form a layered structure (such as $CoPS_3$, $NiPS_3$, etc.).[10] On the other hand, P_2 pairs and metal atoms are located in octahedral and trigonal prismatic coordination, respectively, and the structural units consisting of $P_2S_6^{4-}$ anions can be linked together via S–Sn or S–Pb contacts to constitute the nonlayered structure (like $SnPS_3$ and $PbPS_3$).[11] These structural characteristics result in distinct chemical and physical properties, endowing the $MPCh_3$ materials with rich functionalities for energy storage and conversion.[12] Although $MPCh_3$ nanosheets have been widely studied for electrocatalytic HER,[13] oxygen evolution reaction (OER),[14] and nitrogen reduction reaction (NRR),[15] they are rarely explored for CO_2 ECR. In particular, exfoliating layered and nonlayered $MPCh_3$ nanosheets for CO_2 ECR can be valuable in elucidating the complex active sites-performance relationships for CO_2 ECR on the atomic scale.

The central metal atom interacted with its supporting materials, jointly forming the catalytic active sites in 2D transition-metal catalysts. Accordingly, it is necessary to investigate the effects of the metal and supporting material. Recently, researches addressing the transition metal heteroatom co-doped electrocatalysts in CO_2 ECR give a better understanding of the activity origination.[16] Sulfur (S) atoms exhibit unique properties to regulate the ECR performance by modifying the surrounding structural and electronic environment.[17] Lu and co-workers synthesized a S-doped Ni–N–C catalyst (Ni-NS–C) by a facile method, which achieved a very high CO_2-to-CO conversion efficiency of 99.7 % under −0.80 V vs. RHE. More importantly, their study revealed that the transition-metal, Ni atoms, played as CO_2 ECR active sites, whereas S atoms improved its electrocatalytic activity synergistically by comparing these two S-doped and S-free catalysts.[18] These electrocatalytic CO_2 reduction reactions could also be boosted acquired by using the powerful strategy of sulfur activation in Fe-NS–C,[19] Ni–S–C_T[20] and so on. Furthermore, the different central earth-abundant transition-metal atoms (Mn, Fe, Co, Ni, Cu, Sn···) have been explored for CO_2 reduction in numerous research groups to investigate the effect of central metal on catalytic activity and selectivity.[21] Hence, using different types of $MPCh_3$ nanosheets as models to study the positions of metal atoms or S atoms is of great significance for understanding the mechanism and activity origination of CO_2 ECR.

Among a large variety of nanosheets preparation techniques, liquid-phase exfoliation (LPE) is a widely used method to sonicate the samples in appropriate solvents to induce fragmentation and delamination of nanosheets from their bulk crystal counterparts.[22] However, exfoliation of nonlayered materials using LPE requires breaking chemical bonds rather than just van der Waals forces, which greatly increases the difficulty of exfoliation.[23] Developing effective methods to exfoliate nanosheets from layered and nonlayered bulk $MPCh_3$ is needed for systematically studying the application and reaction mechanism of $MPCh_3$ on CO_2 ECR.

Herein, we have successfully exfoliated uniform and ultra-thin $MPCh_3$ nanosheets from layered $CoPS_3$, $NiPS_3$, and nonlayered $SnPS_3$ bulk crystals via wet-grinding exfoliation (WGE) in the presence of isopropanol (IPA). In this work, we not only efficiently and simultaneously synthesized layered and nonlayered ultra-thin $MPCh_3$ nanosheets, but also revealed the relationship between crystal structures of $MPCh_3$ nanosheets and the performance of CO_2 ECR. The CO_2 ECR properties of all three nanosheets were studied, and it was demonstrated that $SnPS_3$ nanosheets clearly exhibit better performance. The selectivity and reaction rate of HCOOH (i.e., FE_{COOH^-} and j_{COOH^-}) reach 31.6 % and $-7.51\ mA\,cm^{-2}$ at −0.65 V vs. RHE, respectively. As far as we know, this is the first report using $MPCh_3$ to produce HCOOH from CO_2. Density functional theory (DFT) calculations further suggested that the formation of HCOO* via the first proton-electron pair addition is energetically more favorable than COOH*, indicating the dominant role of the HCOOH pathway in CO_2 activation. In addition, both scanning transmission electron microscopy (STEM) characterization and DFT calculations showed that WGE can induce atomic defects in $CoPS_3$ and $NiPS_3$ nanosheets, which is beneficial for CO_2 ECR. This work provides detailed insight into the fabrication of layered and nonlayered 2D nanosheets. It establishes an ideal methodology to design versatile micro-nano structures for understanding the relationships between active sites and catalytic properties at the atomic scale with enhanced catalytic performance.

Results and Discussion

The crystalline structures of monolayer $CoPS_3$, $NiPS_3$, and $SnPS_3$ nanosheet from top and side views are schematically illustrated in Figure 1a. Unlike the layered $CoPS_3$ and $NiPS_3$, the $SnPS_3$ bulk crystals have a distinct nonlayered structure (Figure S1). As reported, $CoPS_3$ and $NiPS_3$ exhibit preferential orientation in the (001) direction owing to the layered structure, whereas nonlayered $SnPS_3$ bulk crystals exhibit a preferential orientation in the (200) direction.[24] It is interesting to notice that in both layered nanosheets, the transition metal elements (Co and Ni) are located between

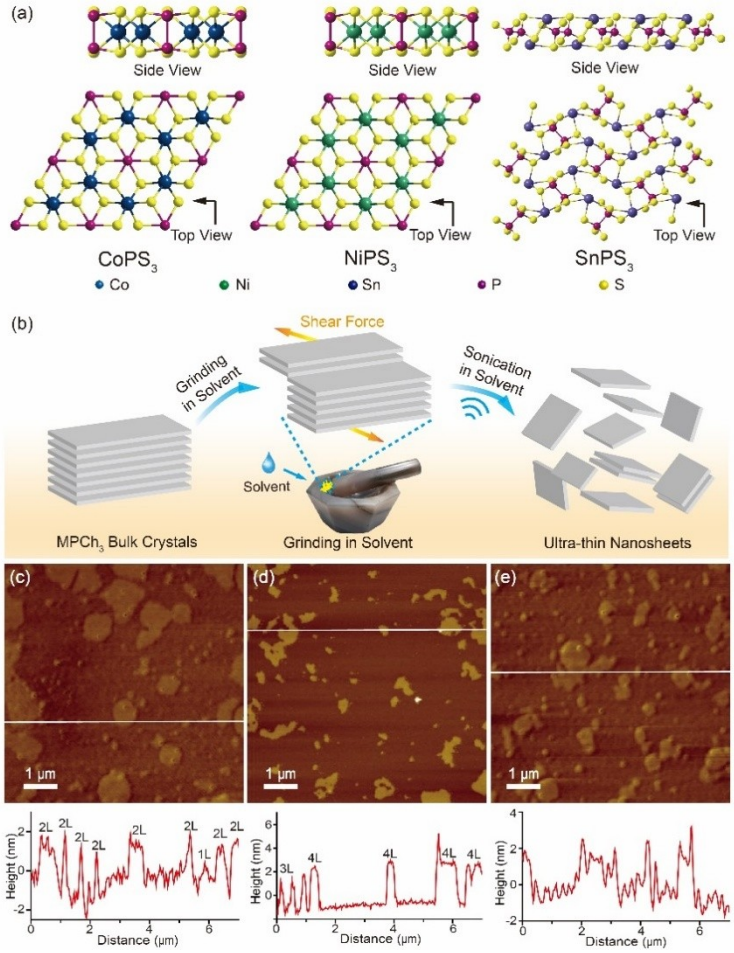

Figure 1. Preparation of $MPCh_3$ nanosheets. a) The crystalline structures of $CoPS_3$, $NiPS_3$, and $SnPS_3$ from top and side views. b) The preparation Scheme for the $MPCh_3$ nanosheets. AFM images and the corresponding height profiles of exfoliated $CoPS_3$ nanosheets (c), $NiPS_3$ nanosheets (d), and $SnPS_3$ nanosheets (e).

atomic layers formed out of nonmetal elements (P and S) and hence are hard to be exposed on the surface, while in the nonlayered $SnPS_3$ nanosheets, the Sn element is located on the surface.

The WGE processes to fabricate $MPCh_3$ nanosheets are schematically shown in Figure 1b. First, we ground the $MPCh_3$ bulk crystals for 30 min using an agate mortar in the presence of IPA. In the second step, the ground samples were added into IPA for sonication and centrifugation to prepare $MPCh_3$ nanosheets dispersions (Figure S2). Compared with the direct LPE, such a pretreatment through grinding produces nanosheets that can significantly reduce the size of $MPCh_3$ bulk crystals (Figure S3) with a shorter sonication time.[25] The mortar generates a shear force along the layer surfaces to break the van der Waals forces or S–Sn bonds to form ultra-thin $MPCh_3$ nanosheets. In this method, IPA was selected as the solvent, as it exhibited good wettability, high viscosity, and appropriate surface energy matching to that of the $MPCh_3$ bulk crystals.

The resulting $MPCh_3$ nanosheets dispersions were transferred to silicon wafers for atomic force microscopy (AFM) investigations (Figure 1c–e), which suggest the thickness of the layered and nonlayered $MPCh_3$ nanosheets are within 3 nm. Given that the thickness of single-layered $CoPS_3$ and $NiPS_3$ nanosheets are about 0.7 nm,[24b,26] the as-prepared layered $CoPS_3$ and $NiPS_3$ nanosheets consist mostly of 1–4 layers according to the thickness distribution (Figure S4). An average lateral size of below 300 nm was observed (Figure S4), consistent with scanning electron microscopy (SEM) images (Figure S5). Furthermore, to the best of our knowledge, this is the thinnest $SnPS_3$ nanosheets achieved from the nonlayered bulk $SnPS_3$. A detailed comparison between the traditional exfoliation methods reported from several literatures and our work has been summarized in Table S1. The results show that we obtained ultra-thin nanosheets with shorter grinding and sonication time without using any toxic solvents, which proves the effectiveness of our WGE method.

We next performed STEM studies to investigate the crystalline quality and atomic structure of as-prepared $MPCh_3$ nanosheets. Figures 2a, d, and g show the overview high-angle annular dark-field STEM (HAADF-STEM) images of the $CoPS_3$, $NiPS_3$, and $SnPS_3$ nanosheets, respectively. Electron energy-loss spectroscopy (EELS) maps

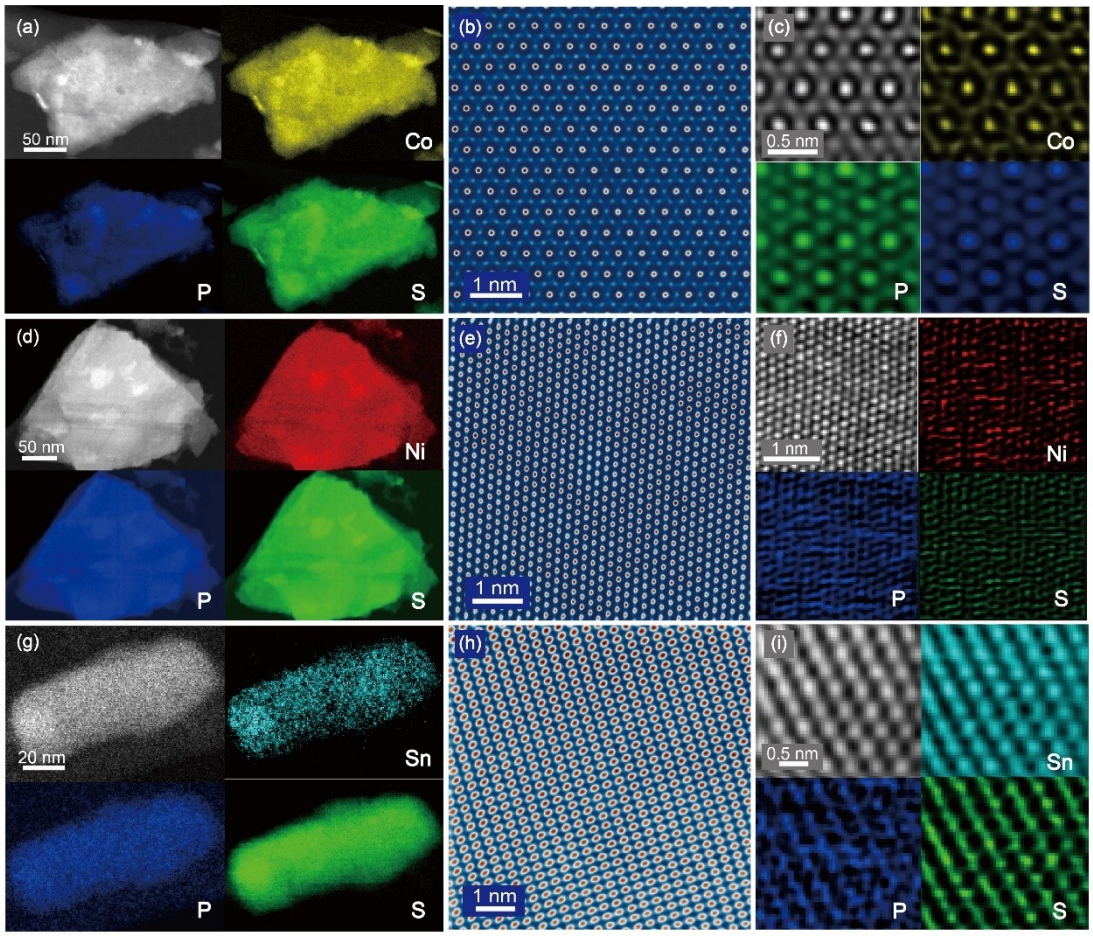

Figure 2. Structure and elemental distribution of the $MPCh_3$ nanosheets. Overview HAADF-STEM images and corresponding STEM-EELS maps (a, d, and g), the colored atomically resolved HAADF-STEM images (b, e, and h), and atomically resolved HAADF-STEM image and corresponding STEM-EELS maps (c, f, and i), a)–c) $CoPS_3$ nanosheets, d)–f) $NiPS_3$ nanosheets, and g)–i) $SnPS_3$ nanosheet.

illustrate that Co/Ni/Sn, P, and S elements are uniformly distributed throughout the entire nanosheets (See information Figure S6 for the corresponding EELS spectra). The colored HAADF-STEM images in Figures 2b, e, and h confirm that the prepared nanosheets preserve an excellent crystal structure even after exfoliation. Moreover, unlike the $SnPS_3$ nanosheets, some point defects appear in the STEM images of $CoPS_3$ and $NiPS_3$ nanosheets, probably due to sonication, grinding, and possible electron-beam damage (Figure S7).[27] It suggests that atomic defects may be more inclined to be formed in layered $MPCh_3$ than in nonlayered $SnPS_3$. We will discuss the effects of vacancies below. Furthermore, atomically resolved EELS maps of $MPCh_3$ nanosheets with layered and nonlayered structures are acquired, revealing the atomic-scale distribution of different atoms (Figures 2c, f and i). Unlike layered $CoPS_3$ and $NiPS_3$ nanosheets, active metal sites of nonlayered $SnPS_3$ nanosheets tend to be exposed on the surface of nanosheets.[11a,24b] X-ray photoelectron spectroscopy (XPS) demonstrates the presence of Co, Ni, Sn, P, and S, and a partially-oxidized surface (Figures S8 and S9). For $CoPS_3$ and $NiPS_3$, there is a slight red shift in the binding energy for the P $2p_{3/2}$ and S $2p_{3/2}$ peaks (131.9 and 162.4 eV for bulk $CoPS_3$, 131.9 and 162.5 eV for bulk $NiPS_3$) compared to bulk crystal (131.3 and 161.8 eV for bulk $CoPS_3$, 130.6 and 161.4 eV for bulk $NiPS_3$),[28] which further confirms the formation of sulfur vacancies in the $CoPS_3$ and $NiPS_3$ nanosheets during grinding and sonication.

To investigate the effect of solvent and grinding on the yield of $MPCh_3$ nanosheets, we employed UV/Vis spectroscopy to study the optical properties of resulting particles, as shown in Figures 3a–c. UV/Vis spectroscopy is based on the Beer–Lambert law, and the absorbance strength can be used to quantitatively characterize the preparation efficiency of WGE. The layered and nonlayered $MPCh_3$ nanosheets were exfoliated using IPA as the grinding solvent with a higher exfoliation efficiency. This is because the grinding can generate shear forces, which facilitates the exfoliation. Moreover, compared with ethanol and acetone, IPA has a higher viscosity to increase the pre-grinding resistance and further increase the shear force along the layer surface.[29] In addition, IPA has a smaller contact angle, which indicates better wettability, proving that IPA is a suitable grinding solvent for WGE of MPCh3 crystals (Figure S10). Under these conditions, the concentration of the $CoPS_3$, $NiPS_3$, and $SnPS_3$ dispersions reach 0.31, 0.65, and 0.22 $mg\,mL^{-1}$,

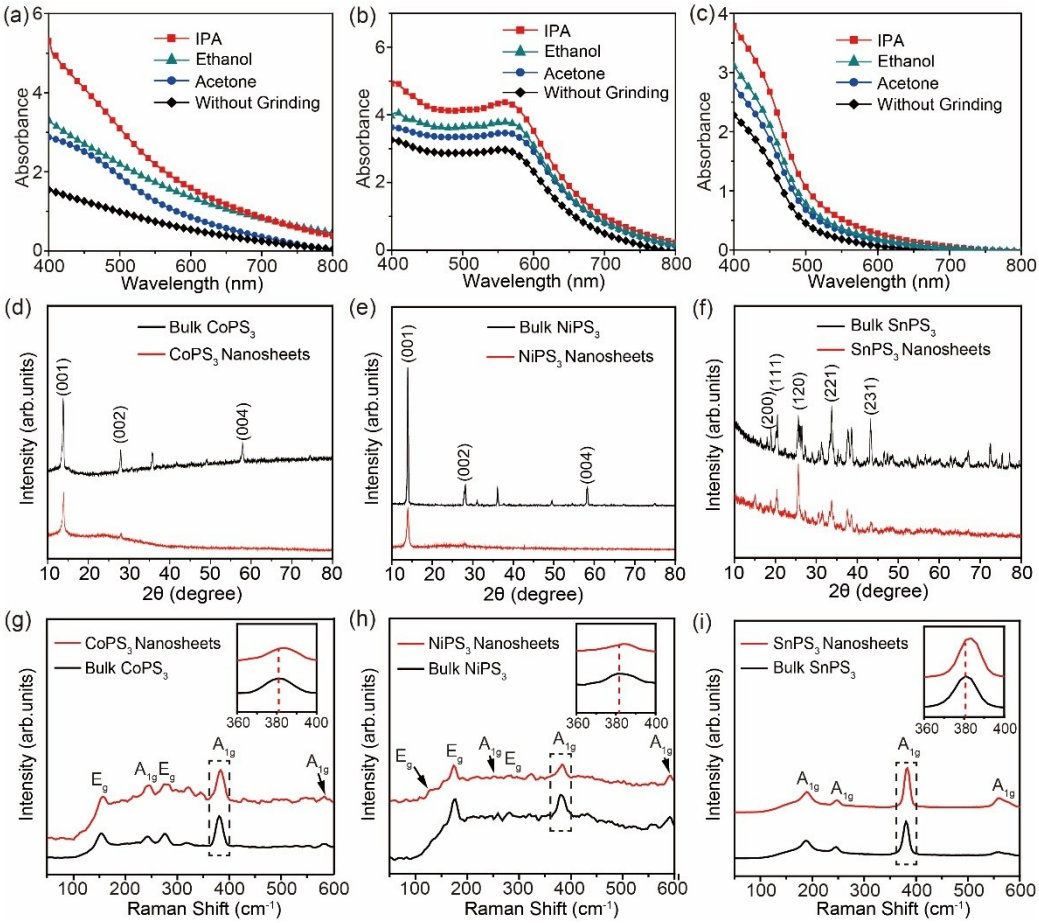

Figure 3. Properties of $MPCh_3$ nanosheets. UV-vis absorption spectra of the $CoPS_3$ (a), $NiPS_3$ (b), and $SnPS_3$ (c) prepared in different grinding solvents (IPA, ethanol, and acetone) and without grinding. XRD patterns of bulk $CoPS_3$ and $CoPS_3$ nanosheets (d), bulk $NiPS_3$ and $NiPS_3$ nanosheets (e), bulk $SnPS_3$ and $SnPS_3$ nanosheets (f) on the glass substrate. Raman spectra of bulk $CoPS_3$ and $CoPS_3$ nanosheets (g), bulk $NiPS_3$ and $NiPS_3$ nanosheets (h), bulk $SnPS_3$ and $SnPS_3$ nanosheets (i), and the corresponding enlarged Raman spectra (inset).

respectively, suggesting a corresponding synthesis yield of 3.1 %, 6.5 %, and 2.2 %, respectively, measured by the commonly used weighing method.[30] We also investigated the effect of acetone as a grinding solvent on the $MPCh_3$ nanosheets (Figure S11). The results show that the grinding solvent has little effect on the lateral size and thickness of the nanosheets.

The crystal structures of $MPCh_3$ were subsequently studied using X-ray diffraction (XRD) with 2θ ranging from 10° to 80°. The peaks in Figure 3d and e can be attributed to the monoclinic $CoPS_3$ (space group $C2/m$) (PDF No.78-0498)[31] and $NiPS_3$ (space group $C2/m$) (PDF No.78-0499).[32] Figure 3f confirms that monoclinic $SnPS_3$ bulk crystals (PDF No.27-1475) have the space group $P2_1/n$.[33] $CoPS_3$, $NiPS_3$, and $SnPS_3$ nanosheets exhibit significantly reduced intensities, which proves the ultra-thin 2D structures. Raman spectra of $CoPS_3$, $NiPS_3$, and $SnPS_3$ are displayed in Figure 3g–i with an excitation laser line of 532 nm. Raman peaks within 50 to 600 cm^{-1} originate from A_{1g} and E_g vibrational modes of the P_2S_6 units. The Raman peaks corresponding to A_{1g} vibrational mode of $CoPS_3$, $NiPS_3$, and $SnPS_3$ nanosheets show a slight shift of 2 cm^{-1} due to the exfoliation of $MPCh_3$ bulk crystals, which demonstrates the successful exfoliation of the nanosheets from layered and nonlayered $MPCh_3$ bulk crystals.[34]

The CO_2 ECR performance of the $MPCh_3$ nanosheets were evaluated using a custom-built flow cell at fixed potentials between −0.45–−0.75 V vs. RHE (Figure 4a).[35] The faradaic efficiency (FE) and current density (j) for all the products with different applied potentials are presented in Figure 4b and Table S2. Hydrogen (H_2) is formed from HER, which is a competing reaction against CO_2 reduction, e.g., $NiPS_3$ and $CoPS_3$ catalysts show insignificant CO_2 ECR activity with the majority product being H_2 (Table S3 and S4), $CoPS_3$ catalysts display higher selectivity towards H_2 at low applied potentials. When the applied potential becomes more negative, the performance of $NiPS_3$ and $CoPS_3$ catalysts is comparable. In addition, the calculated results confirmed that $NiPS_3$ and $CoPS_3$ are better HER catalysts (Figure S12). $SnPS_3$ shows better inhibition of HER as compared to $CoPS_3$. Besides, only CO and $HCOO^-$ are detected when using $SnPS_3$, the FE_{CO} decreased according to the increased overpotential. Importantly, the selectivity and reaction rate of $HCOO^-$ (i.e., FE_{HCOO-} and j_{HCOO-}) for

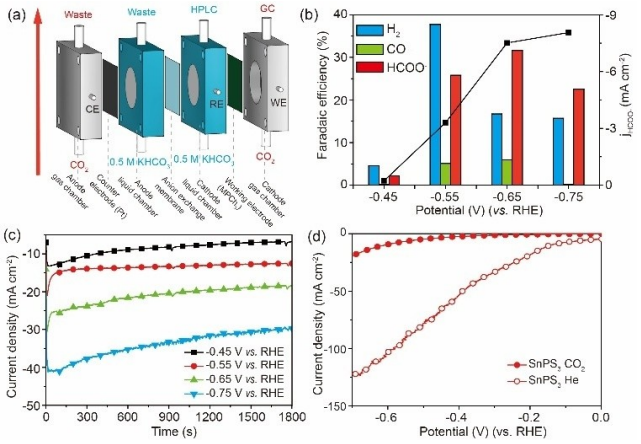

Figure 4. CO_2 ECR performance. a) Scheme of the custom-built flow cell, b) faradaic efficiency of major products and current density of formic acid, and c) chronoamperometry curves using $SnPS_3$ catalyst at different applied potentials, d) LSV curves of $SnPS_3$ catalyst in CO_2-saturated and He-saturated 0.5 M $KHCO_3$ solution.

$SnPS_3$ nanosheets ramps up to 31.6 % and $-7.5\ mA\,cm^{-2}$ at -0.65 V vs. RHE, respectively. As to the best of our knowledge, this is the first experimental report using $MPCh_3$ for CO_2 reduction to $HCOO^-$. The corresponding chronoamperometry curves at different potentials are shown in Figure 4c. The linear sweep voltammetry (LSV) traces performed under a Helium (He) and CO_2-saturated electrolyte solution are depicted in Figure 4d. Under the He atmosphere, the cathodic current density is assigned to HER. The result suggests the cathodic current is severely suppressed in the CO_2-saturated solution.[36] To further verify the active forms of our catalysts, the chemical composition of the $SnPS_3$ catalysts before and after CO_2 ECR were examined by XRD pattern and XPS spectra. In the XRD pattern (Figure S13a), the result shows that the peaks at 30.6°, 32.0°, 44.9° arise from the (200), (101) and (211) planes of tin metal (JCPDS card No. 04-0673)[37] were not detected, only the strong peak of the substrate and the weak peak of $SnPS_3$ were observed. The XPS spectra are consistent with XRD characterization (Figure S13b and c), Sn 3d XPS spectra of $SnPS_3$ catalysts can be deconvoluted into speaks at 486.6, 495.1 (Sn^{4+}), 486.1, 494.4 (Sn^{2+}). No tin metal (485.2 and 493.7 eV) was observed before and after the catalysis.[37] Therefore, the experiment can exclude the emergence of tin metal in the CO_2 ECR.

To further elucidate the mechanism of CO_2 ECR to CO and $HCOO^-$ on the $MPCh_3$ (M = Co, Ni, and Sn) nanosheets, we carried out DFT calculations. CO_2 molecules are initially adsorbed on the $SnPS_3$ surface, on which H_2O molecules dissociate into hydroxyl and hydrogen ions simultaneously. The free-energy profiles for different adsorbed ligands with the lowest-energy pathway on the surface of $SnPS_3$ nanosheets were calculated, as shown in the Figure 5a. The formation of HCOO* via the first proton-electron pair addition is energetically more favorable than that of COOH*, indicating the dominant role of the HCOOH pathway in CO_2 activation. Furthermore, the energy diagram for HER on $SnPS_3$ is also shown in the Figure 5a. To explain the selectivity of the CO_2 ECR, it is widely accepted that the difference between limiting potentials for CO_2 reduction and H_2 evolution ($\Delta U = U_L(CO_2) - U_L(H_2)$, where $U_L = -\Delta G_0/e$) is a reasonable descriptor.[38] A large positive ΔU value denotes a higher selectivity. Therefore, based on our calculations, it is clear that the selectivity of different products follow the trend HCOO- > H_2 > CO, where the corresponding ΔU is 0.36 (between $HCOO^-$ and H_2) and 0.11 (between H_2 and CO) eV, respectively. This is consistent with our experimental observations. In addition, the free-energy diagrams for CO_2 reduction to $HCOO^-$ and CO on $CoPS_3$ and $NiPS_3$ surfaces were also calculated and shown in the Figures 5b–e, with the considered structural geometries for different defect concentrations considered shown in Figure S15. Due to the structural geometry for these two materials, namely the transition metal atoms are (Co and Ni) located between non-metallic element (P and S) layers (as shown in Fig-

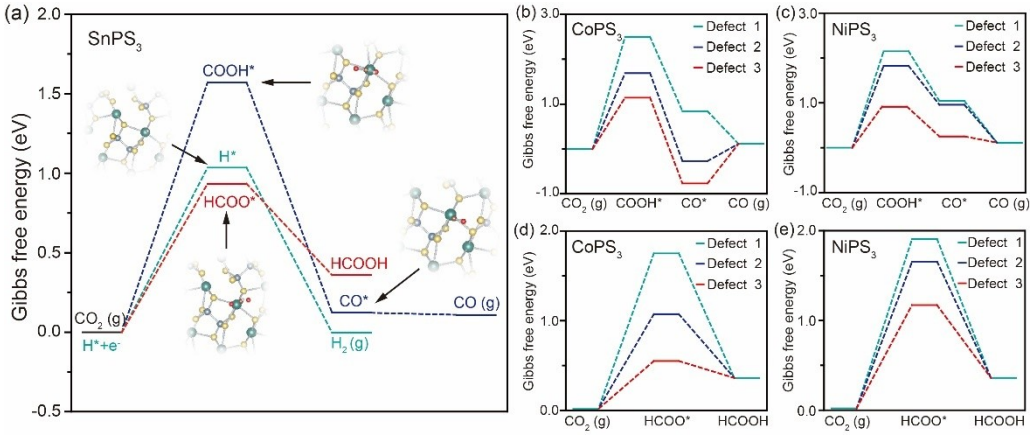

Figure 5. Theoretical investigations. Calculated potential free energy diagrams for HER and CO_2 reduction to HCOOH, CO on the a) $SnPS_3$ surface. The calculated Gibbs free energy diagram for electroreduction to CO on b) $CoPS_3$ surface and c) $NiPS_3$ surface, to HCOOH on d) $CoPS_3$ surface and e) $NiPS_3$ surface.

ure 1a), they are hardly exposed on the surface. Therefore, the perfect monolayers $CoPS_3$ and $NiPS_3$ barely react with the adsorbates, whereas the presence of sulfur vacancies may foster this reaction.[39] The corresponding Gibbs free energies illustrated in Figures 5b–e reveal that the $HCOO^-$ production is more favorable than CO production on $CoPS_3$ and $NiPS_3$ surfaces, especially at higher sulfur vacancy concentrations. This confirms that WGE is a promising method for engineering highly active CO_2 ECR catalysts, like $MPCh_3$ nanosheets by in situ incorporations of sulfur vacancies.

Conclusion

In summary, ultra-thin $MPCh_3$ nanosheets from layered $CoPS_3$, $NiPS_3$, and nonlayered $SnPS_3$ bulk crystals were successfully exfoliated based on the WGE method. $SnPS_3$ nanosheets exhibit enhanced CO_2 reduction with good selectivity towards formic acid production, whereas $CoPS_3$ and $NiPS_3$ display higher selectivity towards H_2. We demonstrated that ultra-thin nanosheets with a thickness of a few atomic layers can be successfully exfoliated for both van der Waals bonded layered and chemically bonded nonlayered $MPCh_3$ materials. The relationship between crystal structures and defects of the resulting $MPCh_3$ nanosheets and their performance of CO_2 ECR were quantitatively evaluated based on experiments and theoretical calculations. The selectivity and reaction rate of HCOOH (i.e., FE_{COOH^-} and j_{COOH^-}) increase step by step, and reach 31.6 % and $-7.51\ mA\,cm^{-2}$ at -0.65 V vs. RHE, respectively, which marks the first report using $MPCh_3$ to produce HCOOH. DFT calculations suggest that the exposed active Sn atoms of $SnPS_3$ nanosheets give rise to enhanced CO_2 ECR with good selectivity against HER and sulfur vacancies are essential for the catalytic properties observed in as-prepared $CoPS_3$ and $NiPS_3$ nanosheets. Our work establishes a feasible method to engineer 2D materials for CO_2 ECR and other electrocatalytic reactions with desired activity and selectivity, which paves the way to tailor the performance of 2D catalytic materials towards future industrial applications.

Acknowledgements

The Center of Micro- and Nanotechnology (ZMN), a DFG-funded core facility at TU Ilmenau, is gratefully acknowledged for professional support. D.R. acknowledges the start-up funding from Xi'an Jiaotong University under the frame of "Young Talent Support Plan" (HG6J002) and Qin Chuangyuan Talent Programme (QCYRCXM-2022-122), H.W. and Y.J. were supported by the China Scholarship Council (CSC) scholarship. Z.S. was supported by ERC-CZ program (project LL2101) from Ministry of Education Youth and Sports (MEYS). B.W. was supported from the OP RDE registration no.: CZ.02.2.69/0.0/0.0/19_073/0016928, funded by the ESF. This work is partially funded through the European Union's Horizon 2020 research and innovation programme under grant agreement No. 823717-ESTEEM3. The authors acknowledge the assistance from Dr. Ming Ma and Wen Yan for HPLC analysis. Open Access funding enabled and organized by Projekt DEAL.

Conflict of Interest

The authors declare no conflict of interest.

Data Availability Statement

The data that support the findings of this study are available from the corresponding author upon reasonable request.

Keywords: 2D Materials · CO_2 ECR · Exfoliation · $MPCh_3$ Nanosheets · Nonlayered

[1] a) Y. Cai, J. Fu, Y. Zhou, Y.-C. Chang, Q. Min, J.-J. Zhu, Y. Lin, W. Zhu, *Nat. Commun.* **2021**, *12*, 586; b) D.-H. Nam, P. De Luna, A. Rosas-Hernández, A. Thevenon, F. Li, T. Agapie, J. C. Peters, O. Shekhah, M. Eddaoudi, E. H. Sargent, *Nat. Mater.* **2020**, *19*, 266–276; c) J. Wu, T. Sharifi, Y. Gao, T. Zhang, P. M. Ajayan, *Adv. Mater.* **2019**, *31*, 1804257.
[2] Z.-Z. Wu, F.-Y. Gao, M.-R. Gao, *Energy Environ. Sci.* **2021**, *14*, 1121–1139.
[3] Y. F. Tay, Z. H. Tan, Y. Lum, *ChemNanoMat* **2021**, *7*, 380–391.
[4] a) S. Zhao, S. Li, T. Guo, S. Zhang, J. Wang, Y. Wu, Y. Chen, *Nano-Micro Lett.* **2019**, *11*, 62; b) H. Liu, Y. Su, Z. Liu, H. Chuai, S. Zhang, X. Ma, *Nano Energy* **2023**, *105*, 108031; c) H. Liu, B. Miao, H. Chuai, X. Chen, S. Zhang, X. Ma, *Green Chem. Eng.* **2022**, *3*, 138–145; d) H. Liu, Y. Su, S. Kuang, E. J. M. Hensen, S. Zhang, X. Ma, *J. Mater. Chem. A* **2021**, *9*, 7848–7856.
[5] K. C. Kwon, J. M. Suh, R. S. Varma, M. Shokouhimehr, H. W. Jang, *Small Methods* **2019**, *3*, 1800492.
[6] Y. Zhou, Z. Wang, L. Huang, S. Zaman, K. Lei, T. Yue, Z. Li, B. You, B. Y. Xia, *Adv. Energy Mater.* **2021**, *11*, 2003159.
[7] Z. Li, L. Zhai, Y. Ge, Z. Huang, Z. Shi, J. Liu, W. Zhai, J. Liang, H. Zhang, *Natl. Sci. Rev.* **2022**, *9*, nwab142.
[8] A. Zhang, Y. Liang, H. Zhang, Z. Geng, J. Zeng, *Chem. Soc. Rev.* **2021**, *50*, 9817–9844.
[9] R. Gusmão, Z. Sofer, M. Pumera, *Angew. Chem. Int. Ed.* **2019**, *58*, 9326–9337; *Angew. Chem.* **2019**, *131*, 9426–9438.
[10] M. Zhu, H. Kou, K. Wang, H. Wu, D. Ding, G. Zhou, S. Ding, *Mater. Horiz.* **2020**, *7*, 3131–3160.
[11] a) B. Scott, M. Pressprich, R. D. Willet, D. A. Cleary, *J. Solid State Chem.* **1992**, *96*, 294–300; b) M. G. Sendeku, F. Wang, Z. Cheng, P. Yu, N. Gao, X. Zhan, Z. Wang, J. He, *ACS Appl. Mater. Interfaces* **2021**, *13*, 13392–13399.
[12] R. Samal, G. Sanyal, B. Chakraborty, C. S. Rout, *J. Mater. Chem. A* **2021**, *9*, 2560–2591.
[13] J. Luxa, Š. Cintl, L. Spejchalová, J.-Y. Lin, Z. Sofer, *ACS Appl. Energy Mater.* **2020**, *3*, 11992–11999.
[14] B. Konkena, J. Masa, A. J. R. Botz, I. Sinev, W. Xia, J. Koßmann, R. Drautz, M. Muhler, W. Schuhmann, *ACS Catal.* **2017**, *7*, 229–237.
[15] B. Vedhanarayanan, C. Chiu, J. Regner, Z. Sofer, K. C. Seetha Lakshmi, J.-Y. Lin, T.-W. Lin, *Chem. Eng. J.* **2022**, *430*, 132649.
[16] X. Wang, Q. Zhao, B. Yang, Z. Li, Z. Bo, K. H. Lam, N. M. Adli, L. Lei, Z. Wen, G. Wu, Y. Hou, *J. Mater. Chem. A* **2019**, *7*, 25191–25202.

[17] a) J. Chen, Z. Wang, H. Lee, J. Mao, C. A. Grimes, C. Liu, M. Zhang, Z. Lu, Y. Chen, S. P. Feng, *Mater. Today Phys.* **2020**, *12*, 100176; b) B. Dembinska, W. Kiciński, A. Januszewska, A. Dobrzeniecka, P. J. Kulesza, *J. Electrochem. Soc.* **2017**, *164*, H484–H490; c) Y. Chen, Y. Yao, Y. Xia, K. Mao, G. Tang, Q. Wu, L. Yang, X. Wang, X. Sun, Z. Hu, *Nano Res.* **2020**, *13*, 2777–2783.
[18] S. Lu, Y. Zhang, M. F. Mady, O. Egwu Eleri, W. Mekonnen Tucho, M. Mazur, A. Li, F. Lou, M. Gu, Z. Yu, *ChemSusChem* **2022**, *15*, e202200870.
[19] F. Pan, B. Li, E. Sarnello, S. Hwang, Y. Gang, X. Feng, X. Xiang, N. M. Adli, T. Li, D. Su, G. Wu, G. Wang, Y. Li, *Nano Energy* **2020**, *68*, 104384.
[20] Y. Zhang, C. Chen, Q.-H. Zheng, Z.-K. Guo, B.-X. Dong, Y.-L. Teng, *ACS Appl. Energy Mater.* **2023**, https://doi.org/10.1021/acsaem.2c02333.
[21] a) F. Franco, C. Rettenmaier, H. S. Jeon, B. Roldan Cuenya, *Chem. Soc. Rev.* **2020**, *49*, 6884–6946; b) C. Xu, A. Vasileff, Y. Zheng, S. Z. Qiao, *Adv. Mater. Interfaces* **2021**, *8*, 2001904.
[22] a) J. Dong, L. Liu, C. Tan, Q. Xu, J. Zhang, Z. Qiao, D. Chu, Y. Liu, Q. Zhang, J. Jiang, Y. Han, A. P. Davis, Y. Cui, *Nature* **2022**, *602*, 606–611; b) H. Wang, W. Lv, J. Shi, H. Wang, D. Wang, L. Jin, J. Chao, P. A. van Aken, R. Chen, W. Huang, *ACS Sustainable Chem. Eng.* **2020**, *8*, 84–90; c) A. G. Kelly, D. O'Suilleabhain, C. Gabbett, J. N. Coleman, *Nat. Rev. Mater.* **2022**, *7*, 217–234.
[23] a) H. Kaur, R. Tian, A. Roy, M. McCrystall, D. V. Horvath, G. L. Onrubia, R. Smith, M. Ruether, A. Griffin, C. Backes, V. Nicolosi, J. N. Coleman, *ACS Nano* **2020**, *14*, 13418–13432; b) H. Kaur, J. N. Coleman, *Adv. Mater.* **2022**, *34*, 2202164.
[24] a) C. C. Mayorga-Martinez, Z. Sofer, D. Sedmidubský, Š. Huber, A. Y. S. Eng, M. Pumera, *ACS Appl. Mater. Interfaces* **2017**, *9*, 12563–12573; b) S. Huang, C. Meng, M. Xiao, S. Ren, S. Wang, D. Han, L. Sun, Y. Meng, *Nano Energy* **2019**, *61*, 462–470.
[25] H. Wang, P. Cheng, J. Shi, D. Wang, H. Wang, J. Pezoldt, M. Stich, R. Chen, P. A. van Aken, W. Huang, P. Schaaf, *Green Chem.* **2021**, *23*, 3642–3648.
[26] S. Xue, L. Chen, Z. Liu, H.-M. Cheng, W. Ren, *ACS Nano* **2018**, *12*, 5297–5305.
[27] J. Jiang, T. Xu, J. Lu, L. Sun, Z. Ni, *Research* **2019**, *2019*, 4641739.
[28] N. M. Latiff, C. C. Mayorga-Martinez, B. Khezri, K. Szokolova, Z. Sofer, A. C. Fisher, M. Pumera, *FlatChem* **2018**, *12*, 1–9, DOI: 10.1016/j.flatc.2018.11.003.
[29] X. Wang, J. He, B. Zhou, Y. Zhang, J. Wu, R. Hu, L. Liu, J. Song, J. Qu, *Angew. Chem. Int. Ed.* **2018**, *57*, 8668–8673; *Angew. Chem.* **2018**, *130*, 8804–8809.
[30] H. Wang, J. Niu, J. Shi, W. Lv, H. Wang, P. A. van Aken, Z. Zhang, R. Chen, W. Huang, *Small* **2021**, *17*, 2102263.
[31] P. Liu, Y. Pu, *Int. J. Hydrogen Energy* **2022**, *47*, 197–202.
[32] R. Dangol, Z. Dai, A. Chaturvedi, Y. Zheng, Y. Zhang, K. N. Dinh, B. Li, Y. Zong, Q. Yan, *Nanoscale* **2018**, *10*, 4890–4896.
[33] S. Haghighat-Shishavan, M. Nazarian-Samani, M. Nazarian-Samani, S. H. Hosseini-Shokouh, T. Maschmeyer, K.-B. Kim, *Chem. Eng. J.* **2022**, *435*, 134965.
[34] F. M. Oliveira, J. Paštika, V. Mazánek, M. Melle-Franco, Z. Sofer, R. Gusmão, *ACS Appl. Mater. Interfaces* **2021**, *13*, 23638–23646.
[35] a) A. M. Asiri, J. Gao, S. B. Khan, K. A. Alamry, H. M. Marwani, M. S. J. Khan, W. A. Adeosun, S. M. Zakeeruddin, D. Ren, M. Grätzel, *J. Phys. Chem. Lett.* **2022**, *13*, 345–351; b) D. Ren, J. Gao, S. M. Zakeeruddin, M. Grätzel, *J. Phys. Chem. Lett.* **2021**, *12*, 7583–7589.
[36] Y. Hori, A. Murata, Y. Yoshinami, *Phys. Chem. Chem. Phys.* **2014**, *16*, 4720–4727.
[37] F. Li, L. Chen, M. Xue, T. Williams, Y. Zhang, D. R. MacFarlane, J. Zhang, *Nano Energy* **2017**, *31*, 270–277.
[38] C. Shi, H. A. Hansen, A. C. Lausche, J. K. Nørskov, *J. Chem. Soc. Faraday Trans.* **1991**, *87*, 125–128.
[39] W. Gao, S. Li, H. He, X. Li, Z. Cheng, Y. Yang, J. Wang, Q. Shen, X. Wang, Y. Xiong, Y. Zhou, Z. Zou, *Nat. Commun.* **2021**, *12*, 4747.

Manuscript received: November 23, 2022
Accepted manuscript online: February 6, 2023
Version of record online: February 27, 2023